Making bioinspired 3D-printed autonomic perspiring hydrogel actuators

Anand Kumar Mishra [1], Wenyang Pan[2,3], Emmanuel P. Giannelis[3], Robert F. Shepherd[1] and Thomas J. Wallin[2,3]✉

To mitigate the adverse effects of elevated temperatures, conventional rigid devices use bulky radiators, heat sinks and fans to dissipate heat from sensitive components. Unfortunately, these thermoregulation strategies are incompatible with soft robots, a growing field of technology that, like biology, builds compliant and highly deformable bodies from soft materials to enable functional adaptability. Here, we design fluidic elastomer actuators that autonomically perspire at elevated temperatures. This strategy incurs operational penalties (i.e., decreased actuation efficiency and loss of hydraulic fluid) but provides for thermoregulation in soft systems. In this bioinspired approach, we 3D-print finger-like actuators from smart gels with embedded micropores that autonomically dilate and contract in response to temperature. During high temperature operation, the internal hydraulic fluid flows through the dilated pores, absorbs heat and vaporizes. Upon cooling, the pores contract to restrict fluid loss and restore operation. To assess the thermoregulatory performance, this protocol uses non-invasive thermography to measure the local temperatures of the robot under varied conditions. A mathematical model based on Newton's Law of Cooling quantifies the cooling performance and enables comparison between competing designs. Fabrication of the sweating actuator usually takes 3–6 h, depending on size, and can provide >100 W/kg of additional cooling capacity.

Introduction

Bioinspiration translates desirable features from natural systems into designs for use in engineered systems[1]. Recently, roboticists developed the materials and manufacturing tools to create robots that replicate the soft tissue systems found in biology[2]. Constructed from soft elastomers, these 'soft robots' mimic animal functions (adaptive locomotion, camouflage, adhesion, sensing and autonomy) that are not possible with conventional rigid robotics[3–5]. Unfortunately, encasing robotic components within elastomeric bodies creates new challenges[6]. In particular, polymers typically possess thermal conductivity that is orders of magnitude below that of ceramics and metals. Thus, to operate at peak power outputs for extended periods of time, soft robots need to employ thermoregulation.

The thermal energy of a body is a measure of its kinetic energy at the molecular scale. These molecular motions govern the observed mechanical, electrical and chemical behavior of matter. Consequently, many systems, both biological and engineered, actively thermoregulate to maintain performance within an acceptable range. The immutable laws of thermodynamics relate heat flow to the work done by a system. A corollary of these laws precludes the existence of perpetual motion machines; the conversion of stored potential energy into useful work cannot be 100% efficient; some remainder is always lost as heat. Hence, work output, and its associated heat production, must be adequately offset by thermal dissipation to avoid the adverse effects of increased temperature[7]. This challenge is particularly compelling when considering the current use of soft robotic power systems that release significant amounts of energy (fluidic compression, exothermic reactions of peroxides and combustion of fuel) necessary for rapid, high-powered actuation[8–11]. Beyond endogenous thermal stress related to power output, soft robots may operate in extreme environments (e.g., temperature, radiation or toxic atmosphere) that are unsafe for living beings[12–14]. In these harsh conditions, thermoregulation is necessary to execute tasks without failure of the robotic subcomponents.

Animals dissipate thermal energy from their bodies to balance heat generated from their basic metabolism and activity levels. While the specific thermoregulatory strategies can be anatomical, behavioral or physiological in origin, animals use four modes of heat dissipation: radiation, conduction,

[1]Department of Mechanical and Aerospace Engineering, Cornell University, Ithaca, NY, USA. [2]Facebook Reality Labs, Redmond, WA, USA. [3]Department of Materials Science and Engineering, Cornell University, Ithaca, NY, USA. ✉e-mail: thomaswallin@fb.com

convection and evaporation. Thermal radiation occurs in all bodies above absolute zero and scales both with temperature to the fourth power and surface area. Because metabolic production scales with mass, radiation is most dominant in small organisms with large surface area–to-volume ratios—larger animals must also use other modes[15]. Behaviorally, animals seek out contact with cold surfaces to conduct away heat. Alternatively, convection is heat transfer mediated by a mobile fluid phase (gas or liquid) near the interface of a body. Evolutionary biologists propose that the anatomical plates in *Stegosaurus* increased convective losses by as much as 50%, and the synergistic effect of vasodilation and ear flapping dissipate 20–50% of the total metabolic heat in elephants through convection[16,17]. Similarly, soft robots based on fluidic elastomer actuators can utilize the circulation of pressurizing fluid to enhance heat exchange[18,19]. However, as first suggested in Newton's Law of Cooling[20], the rate of heat dissipation for conduction and convection depend on the temperature difference between the body and its environment. As such, these mechanisms cannot cool a body below environmental temperature, and their efficacy relies heavily on changing terrestrial conditions. Thus, many land-animal systems use the fourth mode— evaporative water loss (EWL)—to effectively lower temperatures below ambient.

Numerous evolutionary adaptations capitalize on the ubiquity and thermodynamic properties of water for evaporative cooling. Liquid water molecules must absorb significant body heat during vaporization (enthalpy of vaporization: ~40 kJ/mol). Canids adopt rapid, shallow breathing patterns to increase respiratory EWL (REWL) from moist nasal and mouth cavities[21]. Inefficiently, the muscle contractions required for increased respiration also simultaneously increase heat production[22–25]. In another adaptation, domestic pigs can further enhance their cooling capacity from 40 W/m^2 (REWL) to up to 800 W/m^2 by wallowing in mud to trigger cutaneous EWL (CEWL)[26]. When access to pools of water is limited, other mammals promote CEWL physiologically by sweating. The exceptional endurance of horses and humans can be attributed, in part, to their unique capacity for perspiration. Widely distributed networks of sweat glands in these animal systems provide for rapid perspiration and consequently over 20 W/kg of cooling capacity[27–29]. It is important to note that EWL does incur penalties to the organism. Animals need access to sources of aqueous fluids to drink or otherwise replenish lost water[21].

Although previous research used hydrogels (i.e., sponge-like polymer microstructures filled with water) to absorb large amounts of heat, these devices were unable to actively secrete sweat to their surface for vaporization[14,30]. The first robotic example of bioinspired perspiration is Kengoro[31,32]. This humanoid system pumps water through its porous, laser-sintered aluminum skeleton to realize sweating-enhanced performance. In a feat of endurance, the robot did push-up exercises for 11 min without catastrophic thermal failure of the motors. Yet, unlike animal systems, Kengoro's pore dimensions are static, and the source of the fluid is a separate, dedicated hydraulic circuit. By comparison, humans exhibit focal hidrosis, where sweat glands use fluid from the blood to secrete perspiration through temporarily dilated pores. We implemented these biological paradigms by 3D-printing a porous soft-bodied actuator that autonomically (i.e., without external control) perspires[33]. At low temperatures, microscale openings in the polyacrylamide dorsal layer of the actuator remain sufficiently small to allow for hydraulic pressurization and actuation. As temperatures rise above ~40 °C, the poly-*n*-isopropylacrylamide (PNIPAm)–based body collapses as the pores simultaneously dilate to expel the pressurizing fluid from the internal volume. Although this design results in decreased actuation efficiency (i.e., the actuation angle decreases by ~30° with pores), the thermodynamically driven response is reversible. With sufficient evaporative cooling, the rate of water loss will drop as the robotic body cools and the hydrogel networks return to their original conformations.

In our embodiment, the actuating liquid also serves as our perspiration. This strategy combines power transmission with thermoregulation to reduce design complexity and system mass. However, this motif introduces a trade-off in the performance of the robot—water lost as sweat cannot be used for actuation. Untethered operation of the robot requires accounting for these losses or a means of refilling water stores. In addition, as mentioned above, not all sweat is productive; some liquid inevitably falls off the body on to its surroundings. Although this water loss does not cool the robotic hand itself, we demonstrate the ability to thermo-manipulate items by transmitting perspiration across interfaces. This vaporization, combined with conductive heat transfer to the robotic hand, improved the cooling rate of manipulated objects by >200%[33].

Development of the protocol
Materials design and manufacture of an autonomic perspiring hydrogel actuator
Synthetic hydrogels (i.e., hydrophilic polymer networks) are used frequently in bioinspired systems[34,35]. Two classes of hydrogel actuators are common in soft robotics: fluidic elastomer actuators
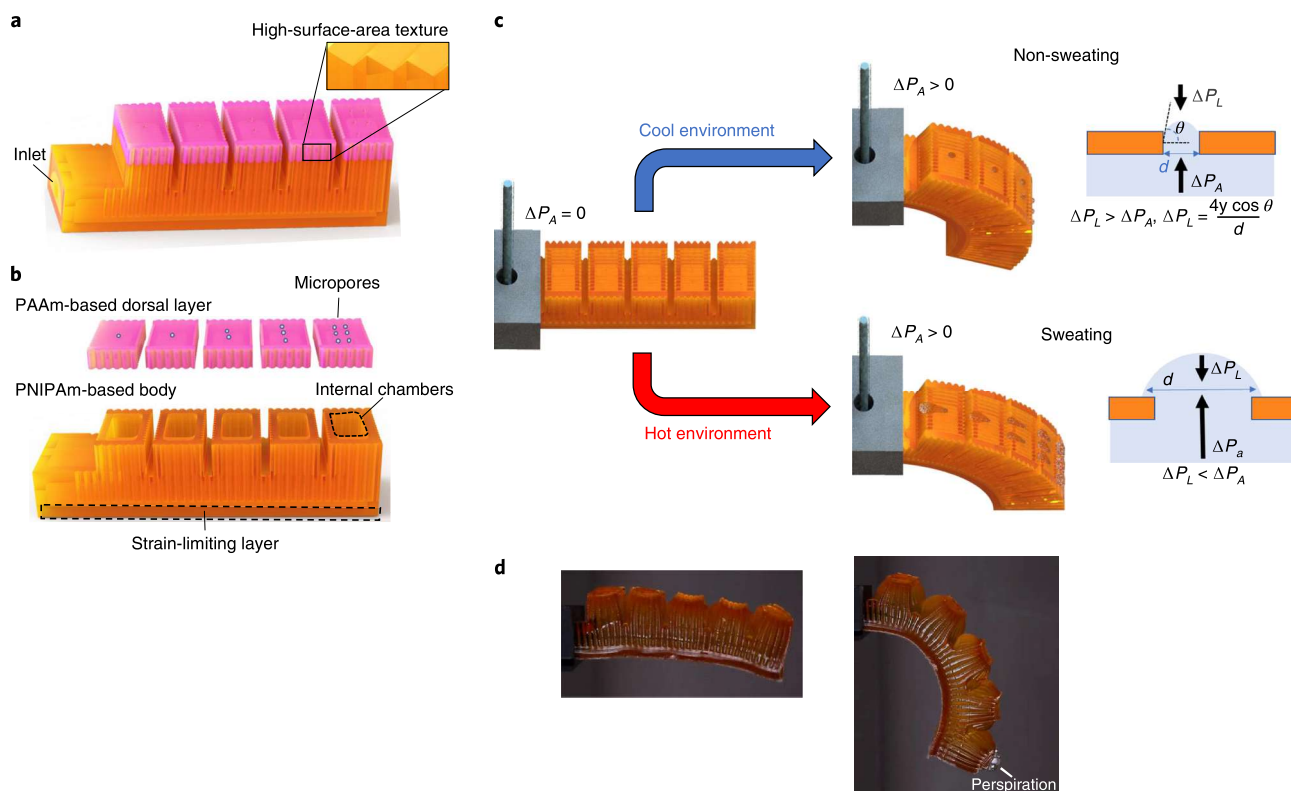
Fig. 1 | Bioinspired 3D-printed hydrogel actuator. a, High-surface-area design actuator with multimaterial printing. **b**, Exploded view of actuator design. **c**, Comparison between pore response and actuator behavior when hydraulically pressurized in different environments. **d**, Actual image of a sweating actuator before and after pressurization. PNIPAm, poly-*n*-isopropylacrylamide. Portions of this figure are reproduced with permission from ref. [33].

(FEAs) and osmotic actuators[36]. Fluidic actuators operate like patterned balloons; during pressurization of internal channels, the elastomeric body changes shape depending on the architectural arrangement of strain-limiting elements (Fig. 1a). By comparison, osmotically driven 'smart' hydrogels reversibly absorb large amounts of solvent directly into the polymer network to change their volume multiple times in response to subtle environmental changes. The energetic balance between the chemical potential energy of the mixture (solvent-polymer system) and the elastic potential energy of the network governs this dynamic behavior[37,38]. When the solvent–gel interaction is favorable, solvent molecules diffuse down the chemical potential gradient to swell the polymer until equilibrating with the elastic potential of the stretched network. If the interaction is unfavorable, the elastic energy dominates, and the gel expels solvent molecules and collapses. In general, FEAs, though more energetically demanding and less efficient, provide for more rapid ($f > 1$ Hz), large-scale, high-force actuation when compared to smart gels[39]. Thus, our design incorporates hydraulically driven FEAs capped by hydrogel layers containing osmotically driven micropores.

In our strategy for autonomic thermoregulation, we require multimaterial fabrication from two hydrogel materials with disparate responses to elevated temperatures. By building the dermal layer from a thermally expanding hydrogel (polyacrylamide (PAAm) based), pore diameters will expand with temperature. For the strain-limiting actuator body, we use a thermally contracting material (poly-*n*-isopropylacrylamide (PNIPAm) based), which results in a decrease in the volume of internal fluidic pathways at elevated temperatures. As shown in Fig. 1b,c, these opposing material responses combine to minimize water loss at low temperatures but promote perspiration at elevated temperatures. The Laplace pressure (ΔP_L) describes the pressure differential sustained by surface tension (g) at a liquid-gas interface of known geometry (defined by contact angle, q, and pore diameter, d). At low temperatures and small pore diameters, the surface tension is sufficient to oppose the applied pressure during fluidic actuation (ΔP_A). At elevated temperatures, the pores dilate and the actuator body simultaneously collapses to increase ΔP_A. Eventually, the surface tension within the pore fails to balance this internal pressure ($\Delta P_A > \Delta P_L$), water flows onto the skin's surface and the robotic system increases CEWL. We note that perspiration occurs at the expense of actuation efficiency; water losses

continue until ΔP_A drops to equilibrate with ΔP_L. Our use of dynamic pores as 'gates' or sphincters is a fundamentally different mechanism than biological perspiration. In human sweat glands, the contraction of myoepithelial cells that surround the secretory coil aid in driving perspiration through ducts to pores on the skin's surface.

We 3D-print our bioinspired actuators by using acrylate-based photopolymer inks and stereo-lithography (SLA). A form of vat polymerization, SLA (also known as digital light processing) systems project a series of photopatterns into liquid photopolymers to create solid objects, layer by layer. Acrylate monomers with different side groups can still copolymerize into a single network; exchanging the composition of the acrylate resin between illumination steps permits robust multi-material construction[40,41]. In SLA, the buoyant support provided by the liquid resin and the high spatial-temporal resolution of light enable printing of soft matter with overhanging geometries desirable in FEAs[42,43]. For autonomic perspiration, the ability to obtain porous features on the order of hundreds of microns is particularly powerful. As ΔP_L is inversely proportional to droplet diameter, not only can small pores sustain the largest actuation pressures without sweating, but high surface area–to-volume ratios promote rapid shape change in smart gels[41]. In addition, we print micron-scale texture on the outer surface to promote 'wetting out' to further enhance CEWL.

Measurement of evaporative cooling capacity

Comparative physiology has a rich history classifying the thermal behavior of animal systems dating back to John Hunter's eighteenth-century distinction between 'warm-blooded' and 'cold-blooded' animals[44]. Since then, numerous studies focused on the role of EWL by tracking the water management as a function of thermal stress. Researchers monitor both water intake (water in food, drinking water and oxidation water) and losses (feces, urine and and respiration)[45]. For small, non-sweating species, standard procedure involves confinement of animals in an enclosed environment under constant air flow. Non-EWLs (e.g., from animal waste) are avoided by coating the bottom surface of the enclosure in oil; experimental protocols then attribute the difference between humidity at the inlet and outlet solely to EWL. For large animals in open environments, REWL is not directly measured but crudely estimated on the basis of extrapolations of short-term respiration rates or local dew point hygrometry. For horses and humans, which exhibit large capacities for perspiration, researchers use direct sweat collection or simply track total weight loss (with metabolic losses estimated via respiration) during exercise[46,47]. However, such methodologies based on EWL probably overestimate the actual cooling performance due to perspiration. In practice, some sweat will inevitably fall off the body before evaporation, particularly during movement.

As an alternative, we developed a protocol that uses thermography to track surface temperatures and, by extension, heat transfer. As mentioned above, all objects radiate energy proportional to the fourth power of the absolute temperature. IR cameras are sensitive to the spectrum of light that corresponds to this thermal electromagnetic radiation (1 μm < λ < 14 μm). IR cameras are now widely available for civilian use at low cost and in handheld form factors. Although capabilities (e.g., field of view, resolution and refresh rate) vary widely with price, the basic operation of thermal cameras is nearly identical to that of popular digital cameras—point and click. The ease in operation and non-invasive, rapid acquisition of local temperatures for large areas makes thermography particularly attractive for soft systems, as traditional rigid sensors (resistive temperature detectors or thermo-couples) distributed about the surface can become burdensome and alter the operational behavior of the robot.

Still, there are limits to thermographic imaging. We estimate that the emissivity of our materials remains constant at ε ~0.9, an assumption that holds for most polymers and biological materials but is often not true for highly reflective metal surfaces. When this assumption is not valid, applications of surface coatings (e.g., black paint) reduce reflectivity, or adjustments to the camera's IR sensors directly accommodate such differences in emissivity. There are also radiative issues with maintaining high resolution under large temperature gradients; the resulting thermographs may overestimate the size of 'hot spots'. Thus, an appropriate camera with sufficient specifications including frame rate, responsivity, noise-equivalent temperature difference, spectral band, minimum resolvable temperature difference and dynamic range is necessary. Unfortunately, the highest-performing cameras are not only expensive but potentially restricted under the International Traffic in Arms Regulations for their applications in weapons systems[48].

Ultimately, this time-dependent thermography data, when used in conjunction with known material parameters, permits modeling of heat transfer in the system (see the procedure for more detail, including the relevant equations). Yet, the problem persists for isolating the contributions from

Table 1 | Printing parameter selection

Modification	Advantages	Disadvantages
Increase [AAm]	Increases gel strength	Increases onset temperature of gel collapse (actuator body material)
	Increases solubility in water	Unreacted monomers require extraction after printing
Increase [NIPAm]	Decreases onset temperature of gel collapse (actuator body material)	Decreases solubility in water
		Decreases gel strength
		Unreacted monomers require extraction after printing
Increase [MBA]	Decreases gelation time	Increases stiffness
		Decreases swelling ratio
		Decreases elongation at break
Increase [riboflavin]	Decreases gelation time	Decreases resin stability
Increase [hydroquinone]	Increases resin stability	Increases gelation time
Increase [water]	Decreases viscosity of resin	Increases gelation time
	Decreases stiffness	Decreases strength

perspiration and evaporation from the other heat transfer modes, particularly convection. Traditional experiments minimize convective losses by making the measurement under vacuum, a situation which is not representative of terrestrial conditions. Instead, our protocol simply conducts measurements for equivalent systems under different conditions (e.g., sweating and non-sweating and free and forced convection), models the temperature drop according to Newton's Law of Cooling and infers the contributions from the different modes by the comparative performance. In addition, although we focus on heat dissipation, our proposed procedure can also measure the heat generated during active robotic operation.

Experimental design
Manufacturing and materials
Printing. Although there are now numerous commercial offerings for inexpensive desktop SLA printers, we chose an Autodesk Ember. This system contains a LED-based UV ($\lambda = 405$ nm) projector with an irradiative power, H_e, of ~22.5 mW/cm^2 for 1,280 by 800 pixels that cover a 64 mm by 40 mm build area.

Chemistry. Designing a 3D-printable hydrogel chemistry for autonomic perspiration requires balancing numerous engineering trade-offs in processability, mechanical performance and dynamic response. In simple formulations, these resins usually contain photopolymerizable monomers (acrylates; e.g., acrylamide (AAm) and *N*-isopropylacrylamide (NIPAm)), multifunctional cross-linking species (e.g., *N,N'*-methylene-bisacrylamide (MBA)), a photo-initiating system (riboflavin and triethanolamine (TEOHA)), a radical stabilizer (hydroquinone) and a suitable solvent for all components (water). However, the selection and relative amounts of these components can drastically alter performance as shown in Table 1. For example, increasing the amount of crosslinker enables rapid gelation during printing, but the increased crosslink density also makes the resulting polymer more brittle and reduces the dynamic swelling response.

Resin formulation is often an iterative process that should incorporate considerations from the mechanical design (i.e., target resolution specifications) and performance of the printed object (i.e., ultimate strain during operation). Table 2 shows a representative formulation of AAm- and NIPAm-based resins described in previous work[49].

Characterizing the dynamic response of the hydrogel
When designing sweating machines based on smart hydrogels, an understanding of the underlying dynamic response of the material is critical. Hydrogel swelling is governed by a thermodynamic balance between the solvent-polymer interaction that promotes swelling and the elastic energy of the

Table 2 | Representative recipes for 3D-printable hydrogel resins

AAm-based resin (dorsal layer)	NIPAm-based resin (body of actuator)	Units
25	3.5	g AAm
0	17	g NIPAm
0.542	0.33	g MBA
0.2	0.2	ml of hydroquinone solution (1 mg/ml H_2O)
30[a]	33.5[a]	ml H_2O
0.2	0.2	ml of riboflavin solution (1 mg/ml H_2O)
1.8	1.8	ml of TEOHA solution (0.3 g/ml H_2O)

[a]When adding dye or nanoparticles, decrease the amount of water to maintain a consistent total volume.

polymer network that favors collapse. As such, the swelling behavior changes drastically based on the solvent composition and temperature. In addition, swelling is mediated by the diffusion of solvent from the surroundings across the polymer-solvent interface; there is a strong dependence on swelling kinetics and the hydrogel surface-to-volume ratio (SA:V). Thus, one needs to conduct time-dependent swelling experiments across various experimental conditions that replicate likely environmental ones. We quantify the degree of swelling in terms of mass (gravimetric) and dimensional change (direct imaging), both involving simple methods accessible to researchers with an undergraduate level of training. Appropriate planning can enable simultaneous collection of the two data streams.

Comparative analysis of cooling capacity
In real world operating conditions, the sweating actuators not only shed heat by vaporizing water but also passively cool via radiative, conductive and convective losses. Beyond being a conventional heat transfer mode, convective air currents can also enhance EWL by decreasing the vapor pressure (Bernoulli's effect) and reducing relative humidity immediately above the surface. Thus, the rate of evaporation, and thereby the cooling capacity of a sweating robot, depends greatly on the local motion of air. Unfortunately, 'free convection' occurs naturally in terrestrial environments as a result of temperature gradients; warm gases near the hot surface become less dense and rise to create currents. This phenomenon is dependent on both the motion and the geometry of the body, which limits the utility of comparing the performance of sweating robots. As an alternative, we suggest experimentally creating a sufficient 'forced convection', which dominates the intractable contribution from 'free convection'. To further isolate the vaporization of sweat, we also recommend conducting numerous comparative cooling experiments, particularly comparing the results from sweating robots and their non-sweating counterparts. Among these numerous experiments, the change in body temperatures as a function of time can be fit to a first-order differential based on Newton's Law of Cooling and quantified by using a lumped parameter analysis. Refer to the procedure for more information.

Modifying the procedure to improve performance
Opportunities to improve thermoregulatory performance exist by using pressurizing fluids beyond pure water. For example, salts or other ions can be used to modulate both the heat of vaporization and the boiling point. The use of organic solvents may also lower the boiling point to enhance low-temperature evaporation and thereby maintain a lower body temperature. However, such modifications may also alter hydrogel swelling behavior and thereby pore dilation and contraction. In addition, the thermodynamic calculations need to include the composition-dependent enthalpy of the vaporization.

Soft robots operating in diverse environmental conditions will need to thermoregulate to offset heat generated during periods of high-power output. Similar to animal systems, autonomic perspiration offers a means to rapidly cool body temperature in simple polymeric actuators. We envision a future in which robots attain a higher autonomy, and we expect these advances to require devices with more sophisticated forms that exceed the simple manifestation above. For example, vertebrates

are composed of both stiff skeletons and soft tissues that enable load bearing activities and high force 256
generation, tasks that remain difficult for conventional soft hydrogel actuators. Future robots may use 257
a thin perspiring hydrogel skin that encapsulates more robust components. In addition, our multi- 258
functional design uses the actuating fluid as the perspiration, which reduces design complexity and 259
weight but incurs obvious penalties: sweating requires some actuation pressure, and actuation effi- 260
ciency decreases as the pores dilate. We propose an alternative strategy where a dedicated micro- 261
fluidic system for sweating is 3D-printed on top of the hydraulic system for actuation. Regardless of 262
the design and manufacturing specifics, this protocol provides guidelines for quickly measuring 263
surface temperature and develops a mathematical model for evaluating the thermoregulatory 264
performance among competing systems. 265 Q9

Materials
266

Reagents
267
- AAm (Sigma-Aldrich, cat. no. A9099) 268
- NIPAm (Sigma-Aldrich, cat. no. 731129) 269
- MBA (Sigma-Aldrich, cat. no. 146072) 270
- TEOHA (>99%; Neta Scientific, cat. no. OAK-242387) 271
- Hydroquinone (99%; Sigma-Aldrich, cat. no. H9003) 272
- Riboflavin (>99%; Neta Scientific, cat. no. OAK-21910) 273
- Deionized water 274
- (Optional) iron oxide nanoparticles (see previous work for synthesis)[33] 275
- (Optional) Carbon urethane methacrylate 276
- Cyanoacrylate superglue (McMaster Carr, part no. 74765A63) 277

Equipment
278
- Autodesk Ember 3D printer 279
- (Optional) Carbon M1 printer 280
- Thermal camera (FLIR E4) 281
- DSLR camera (Canon EOS 80D, 24.2 megapixels) 282
- Hot plate (Corning PC420-D) 283
- Analytical balance (Mettler Toledo XPR3003S) 284
- Syringe pump (New Era Pump Systems Inc. NE-1000) 285
- Personal computer 286
- Tygon tubing (McMaster Carr, part no. 6516T11) 287
- Syringe with Luer lock (McMaster Carr, part nos. 7510A802 and 7510A807) 288
- Pressure sensor (0–100 PSI; Transducers Direct LLC, TDH30-CG-0100-03-D004) 289 Q10
- Multi-channel data-acquisition module (National Instruments USB 6501) 290
- Air circulator fan (Honeywell Inc. HT900) 291
- (Optional) Uni- and bidirectional adhesive tape (3M) 292
- (Optional) 20-ml glass vials 293
- 100- and 500-ml glass beakers 294
- Ruler 295

Software
296
- Autodesk Print Studio 297
- ImageJ1.X 298
- Dassault Systems SolidWorks 2018 299
- National Instruments LabVIEW 300
- FLIR Tools 301
- Mathworks MATLAB 302

Procedure
303

Bioinspired actuator design
304
1   Design the FEA body in 3D modeling software. In our case, we used SolidWorks 2018. Although 305
the specifics of the design depend on application, conventional FEAs require an inlet, strain- 306
limiting elements and internal fluidic chambers. For our rectangular finger-like actuators, we start 307

with an outer dimension of 60 mm × 16 mm × 17 mm (see Supplementary Fig. 1 for design 308
schematics and reference [50] for design files). 309

2   For the inlet to couple with 3-mm tubing, create a 3-mm long cylindrical hole in the actuator with a 310
diameter of 2.59 mm. The soft body of the actuator can accommodate the wider tubing and enable 311
a frictional fit. 312

3   To maximize actuation amplitude while minimizing local strains, we incorporate five consecutive 313
fluidic chambers (internal volume of 5.5 mm × 14 mm × 12 mm) connected to this inlet. We 314
enclose each of these 'bellows' in a 2-mm thick wall. Each chamber is 1.5 mm apart; when inflated, 315
adjacent chambers expand, contact each other and promote bending. 316
▲ CRITICAL STEP   To aid in printing the overhanging features of these chambers, we recommend 317
filleting the edges. We found a fillet diameter of 5.5 mm sufficient. 318

4   Our desired actuation mode replicates flexion of the finger. Thus, the ventral plane of the actuator 319
needs to be a strain-limiting element. We chose to incorporate a thicker (2-mm) layer of the 320
PNIPAm-based material to direct actuation. 321
▲ CRITICAL STEP   For an actuator body composed of a single material, the thickness of the bending 322
plane should be greater than the actuator wall thickness. 323

5   In the design software, insert pores through the dorsal layer to the internal fluidic channels with the 324
desired size and shape. For our PAAm-based surface, we found that circular pores <100 microns in 325
diameter are desirable. At this scale, we observe fluidic actuation with minimal water loss when 326
closed at low temperatures, but sufficient pore dilation for perspiration at elevated temperatures 327
(see Characterizing the dynamic response of the hydrogel). To mitigate fluidic energy loss, we 328
recommend a low density of pores near the inlet. In practice, we placed one pore in the first 329
chamber, six pores in the final chamber and two pores in each of the intermediate bellows. 330
▲ CRITICAL STEP   The pore shape, size and density in the actuator design affects printability, 331
autonomic thermal response and actuator efficiency. We conducted an iterative design-feedback 332
cycle that evaluated pore area change (see Characterization of smart materials for autonomic pores) 333
and actuation amplitude (see Mechanical performance of the actuator) as a function of 334
temperature. 335
? TROUBLESHOOTING 336

6   Add texture onto the actuator body to increase the cooling rate. On the basis of the designed 337
iteration (Supplementary Fig. 2), we selected the pyramid (isosceles triangle with a constant depth, 338
0.5-mm sides and 1-mm base; Fig. 1a) to increase total surface area by 16.7%. 339
▲ CRITICAL STEP   We did not add extra material onto the actuator body; instead, we subtracted 340
material with the ‚cut tool‘ and repeated this action with the linear pattern tool in SolidWorks. This 341
method reduces the thickness of the structure without compromising the structural stability. In 342
addition, while a finer texture would possess a greater SA:V ratio (1.32 times as much than without 343
texture), we found rough features <500 microns difficult to rapidly print. 345

Printing of polymeric devices (print times are proportional to object height, ~1 cm/h) 346
▲ CRITICAL   The method described here is one option of many numerous potential strategies that could 347
result in a robotic system with autonomic sweating. Other manufacturing methods (direct ink writing, 348
ink jetting and molding) and other material chemistries may obtain similar performance. As such, the 349
following steps are not prescriptive but serve as a guide. Refer to Experimental design for more 350
information. 351

7   Prepare ≥50 ml of resin by combining all components (Table 2) until dissolved. To maximize 352
stability of the resin, store all chemicals at low temperature in opaque, sealed containers. For best 353
results, add the photoinitiator system (e.g., riboflavin and TEOHA) to the resin immediately before 354
use. Minimize ambient exposure to light by working quickly in a dark room. Resin preparation 355
should take <20 min for a single undergraduate researcher. 356

8   In an initial experiment, determine exposure settings for the materials by generating a 'working 357
curve' (i.e., cure depth versus exposure dosage)[49]. Briefly, this experiment measures the height of 358
cured objects from single exposures of increasing time scales. We recommend placing a vat of resin 359
above your light source and exposing for different periods of time (e.g., 10-s intervals). After 360
exposure, remove the uncured resin and immediately determine the height of the solid material. 361
Because hydrogel materials are probably too soft to be practically measured with a caliper, we 362
recommend optical measurements of the height (see Pore dimensions via image analysis). Plot the 363
height of the object (or cure depth, C_d) as a function of the log of the exposure dose (log H_e). 364

Extrapolate the exposure dosage necessary for the target layer height and use this value to guide the 'exposure time'. For our system, we use 22 and 59 s of exposure for AAm- and NIPAm-based materials (layer height = 250 μm), respectively.

9   Prepare the print file from the associated CAD file (.stl or .obj). In the printer's software, align and orient the design to minimize the total number of layers (a proxy for print time) and avoid abrupt changes in cross-sectional area between layers, where possible. If necessary, add sacrificial supporting structures as recommended by the software. In general, it is best to place a large, flat area of the part directly on the build head to minimize the need for supports. Select a layer height that is less than the minimum desired z-resolution. In our system, we chose a layer height of 250 microns. After defining the necessary parameters, export the print file to the printer. In our case, Print Studio software (Autodesk) generates a zipped file (.tar.gz) that can be directly read by an Autodesk Ember printer.

10   Pour the resin into the vat and begin printing. For multimaterial prints, determine when to pause the print, raise the build stage and change the resin stock.

     ▲ CRITICAL STEP During resin replacement, reduce material contamination by removing all unreacted liquid from the object and vat, and avoid introducing alignment issues that occur when the build stage is shifted.

11   (Optional) For longer prints, it can be time consuming to continuously monitor print progress for resin exchange at the appropriate layer. We recommend adding a 'pause' or 'wait' step to signal the need for this material swap. The actual modifications will vary with the proprietary software. We provide two examples of ways this can be done.

     (A) **Manual layer detection**

        (i) To increase the 'wait' time for the desired transition layer, extract the zipped (.tar.gz) print file twice. In the resulting directory, there will be a series of images corresponding to each sliced layer as well as a 'printsettings.txt' file.

       (ii) Add a 'layersettings.csv' file to this directory. The comma-separated values should contain an initial heading row that starts with 'Layer' and then includes a cell with each 'Model' parameter from the printsettings.txt file.

      (iii) In the next row, below 'Layer', enter the appropriate layer number for the material swap, and below 'ModelPressWaitMS', enter 60,000 to create a 60-s wait. Repeat as necessary in other rows for additional layers, leaving all other cells unmodified.

       (iv) After saving, select all files (slices, printsettings.txt and layersettings.csv), zip all files and export to the Ember printer as before.

       (v) During printing, there will now be a prolonged 'wait' period of 1 min at the desired layer. Press the 'Pause' button on the front of the printer. After the build stage rises from the vat, swap the resin and press the 'resume' button. Repeat as necessary.

     (B) **Automatic layer detection**

        (i) Alternatively, to add a 'pause' at the desired layer, connect to the Ember printer by using the USB port. Write a script that periodically checks the status of the printer by using cURL, a free command line tool:

```
>curl -d "command=GETSTATUS" -X POST (http://192.168.7.2/command)
```

       (ii) Have the script parse the output to get the layer number, and at the appropriate layer, the script should issue a pause command:

```
>curl -d "command=PAUSE" -X POST (http://192.168.7.2/command)
```

          The printer should now raise the build stage out of the vat and pause indefinitely until a user presses the 'resume' button after exchanging the resin. Repeat as necessary.

12   If the print is successful, remove the object from the build stage. When not in use, store all hydrogel objects in a sealed plastic bag to reduce water losses. If the print failed, identify the failure mode and address the issue with changes to the print parameters or material resin.

Characterization of smart materials for autonomic pores ● Timing ~24 h

▲ CRITICAL   The purpose of these steps is to find out how the hydrogel expands and contracts under different environmental conditions.

    We quantify the degree of swelling in terms of mass (gravimetric) and dimensional change (direct imaging), both involving simple methods accessible to researchers with an undergraduate level of training. Appropriate planning can enable simultaneous collection of the two data streams.

13   Prepare hydrogel samples in a defined geometry that approximates the actuator dimensions   424
(pore dimension, layer thickness and SA:V ratio). We chose to fabricate rectangular prisms   425
(10 mm × 10 mm × 2 mm) with four holes (pores) through the thinnest dimension. The initial   426
shape and size of these pores can be varied as needed by simply altering the printed design.   427
▲ CRITICAL STEP The hydration state of hydrogels often changes under ambient conditions.   428
Minimize exposure to the atmosphere, by conducting measurements rapidly and, when possible,   429
store in an enclosed atmosphere (e.g., a plastic bag).   430

14   Immediately weigh the sample and take an image of all pores with a known scale to determine the   431
initial as-fabricated state. Micron-scaled pores may require a microscope or macro lens to resolve   432
all features. For recording mass, we recommend a precision balance with a sensitivity of ≤1 mg   433
(Mettler Toledo MS403S).   434
▲ CRITICAL STEP When using simple photography methods, include a reference object of known   435
length, preferably a ruler in the field of view. Adjust the lighting such that pores are clearly   436
resolvable in all images.   437

15   Place the sample in the desired environments. We selected pure water at temperatures from 20 °C   438
to 80 °C in 10 °C increments.   439

16   At defined times, remove the samples from the environment. Place the sample on a lint-free non-woven   440
wipe to remove any unbound solvent from the surface. Rotate the sample until all sides are dried.   441

17   Immediately after drying the sample, weigh the sample and take images (microscopy or   442
photography) of all pores with a known scale. Ensure that sample identification is either directly   443 Q13
evident in the image or present in the file's metadata.   444

18   Repeat Steps 2–5 as needed. The spacing of time intervals can increase throughout the   445
measurement, because hydrogel swelling exhibits logarithmic behavior until equilibrium is reached   446
(often after 24 h).   447
▲ CRITICAL STEP Swollen hydrogels can be delicate. If the gel becomes damaged in any way during   448
manipulation, discard and repeat the measurement on a freshly fabricated sample.   450

Pore dimensions via image analysis   451

▲ CRITICAL There are numerous image processing software packages. Below, we provide the general   452
procedures for image analysis, but will focus on methods compatible with ImageJ1.X, a popular public   453
domain, open-architecture tool.   454

19   Collect all images as outlined in Characterization of smart materials for autonomic pores.   455

20   If unknown, determine the length scale of pixels. Although many microscopes have proprietary   456
software that converts pixels to distance, this feature is not available in common cameras. Using the   457
'straight line' tool, draw a line that connects two points separated by a known distance (e.g., 1 cm)   458
along the reference object (above). Go to *Analyze → Set Scale* and enter the known length of this   459
line with a pixel aspect ratio of 1. This process will convert the pixels to dimensions of length.   460
Quantify the number of pixels within the pore area. For individual pores, this can be done   461
manually. With the freehand selection or elliptical selection tools, enclose the pore. Go to *Analyze →*   462
Measure (Ctrl+M) to obtain the measured pore area. For batch processing of multiple pores, it is   463
also possible to collect area data via thresholding. Go to *Image → Adjust → Thresholding* and adjust   464
the histogram until fully selecting all pores in the original image. Apply the threshold to convert the   465
image into black and white. Next, select *Analyze → Analyze Particles*, which returns the measured   466
areas for all identified pores.   467

21   Repeat measurements to collect data for a statistically significant number of pores (at a minimum, $n > 7$).   468

22   These measurements yield the kinetics of hydrogel response under varying conditions. In ideal   469
autonomic perspiration, the smart material has pores that rapidly dilate at elevated temperatures   470
but remain sufficiently closed at desired operating conditions. Modify the material composition   471
and/or pore design until these targets are met.   473

Mechanical performance of the actuator   474

▲ CRITICAL For unidirectional finger-like FEAs, it is useful to characterize the bending angle as a   475
function of actuation pressure (or volume). More advanced actuation systems (i.e., multimodal   476
actuators) will probably require modifications to this protocol and additional experiments to fully   477
quantify mechanical performance.   478
We note that our sweating strategy incurs penalties in FEA performance. Particularly, the presence of   479
the pores can mean that the material fails to maintain large pressure differentials during fluidic   480

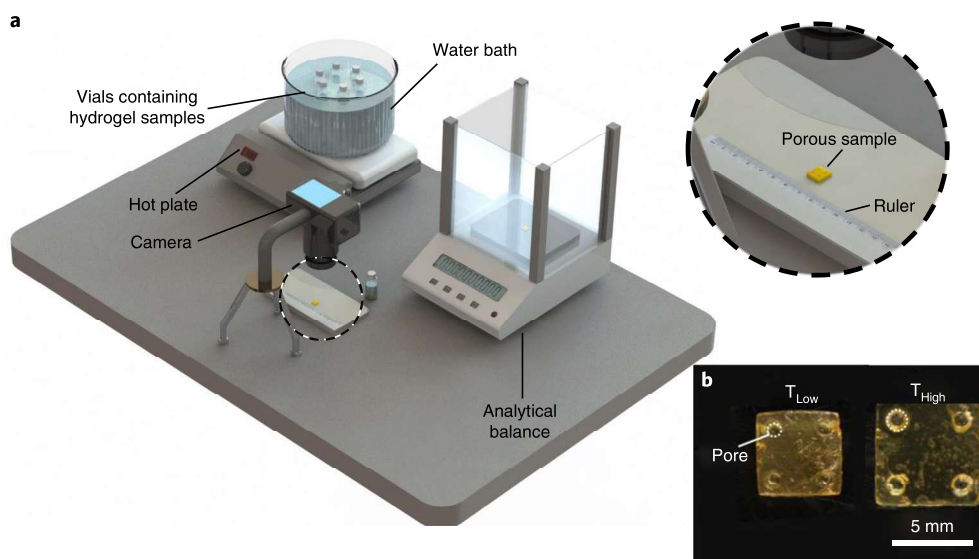**Fig. 2 | Characterization of smart pores. a**, Experimental setup for pore analysis. **b**, Representative images of porous hydrogels at different temperatures. Portions of this figure are reproduced with permission from ref. [33].

actuation (Fig. 2). To quantify this inefficiency, we recommend printing an identical non-sweating actuator (i.e., without pores) and repeating these measurements for comparison.

23 Couple fluidic tubing (Tygon, 3.175-mm o.d., 1.58-mm i.d.) to the actuator's inlet. We found it easiest to create a leak-free seal by applying a liquid adhesive to the tubing before insertion. Both cyanoacrylate glue and excess hydrogel resin (with subsequent UV exposure) are suitable adhesives.
    ▲ CRITICAL STEP The hydrogel actuators are often very delicate and tacky. During this process, handle the actuator gently and use non-stick surfaces, where possible.

24 Secure the base of the actuator assembly to a stand such that the actuator can bend freely. As shown in Fig. 3a, we 3D-printed (Carbon M1 printer) stands and chassis out of rigid commercial materials (Carbon urethane methacrylate) to both mechanically secure the actuator and provide fluidic routing in the multi-fingered devices (see Supplementary Figs. 3 and 4 for design schematics and refs. [46,50]). Then, set up a high-resolution digital camera (Canon EOS 80D, 24.2 megapixels) with a field of view that captures the entire range of motion of the actuator.

25 Connect the fluidic control equipment. We built a volumetric control system by using a syringe, pressure sensor, manual on/off valve, syringe pump (New Era Pump Systems Inc. NE-1000) as shown in Fig. 4. When attaching the system to the Tygon tubing, we recommend a syringe with a Luer lock connection and the appropriate coupling hardware.

26 Use LabVIEW software to control the syringe pump while simultaneously monitoring the pressure sensor and video recording the actuator motion. We collected these data while injecting fluids at a rate of 5 ml/min.

27 Analyze the bending angle as a function of actuation state (volume and pressure). To enable rapid processing, we developed a separate program in MATLAB. The full code is available in the Supplementary Information; briefly, this program first imports the video in MATLAB and separates each frame. Next, in each image, the algorithm detects the top and bottom edges of the actuator (Supplementary Fig. 5). The program automatically measures the angle between a line of interest (i.e., the top edge) and a reference line (i.e., the bottom edge at t = 0).
    ▲ CRITICAL STEP Avoid bursting the thin walls of the actuator by over-pressurization.

Thermoregulatory performance of sweating actuators
▲ CRITICAL Fabricate a geometrically identical but non-sweating actuator by removing the pores from the design. The purpose of these steps is to find out whether perspiration occurs when the material is hot, and whether this perspiration results in cooling.

28 Begin by equilibrating the actuator assembly, including the water reservoir in the syringe, at an elevated temperature. This step minimizes any thermal gradients within the body and surface of the actuator at the start of the experiment. Perform the sweating tests, first on the single actuator and
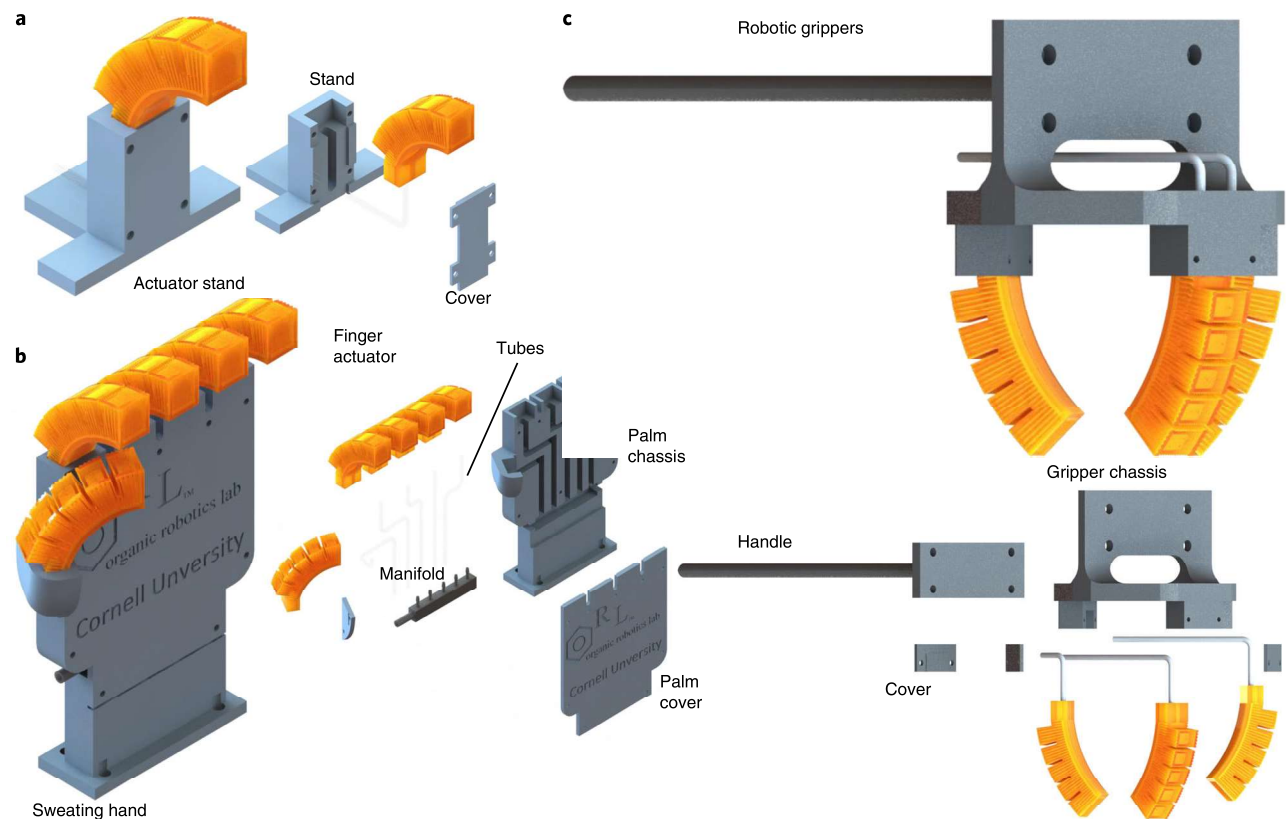
Fig. 3 | Robotic systems for performance testing. a, Single actuator assembled in a 3D-printed stand. **b**, Anthropomorphic soft hand. **c**, Robotic three-point gripper.
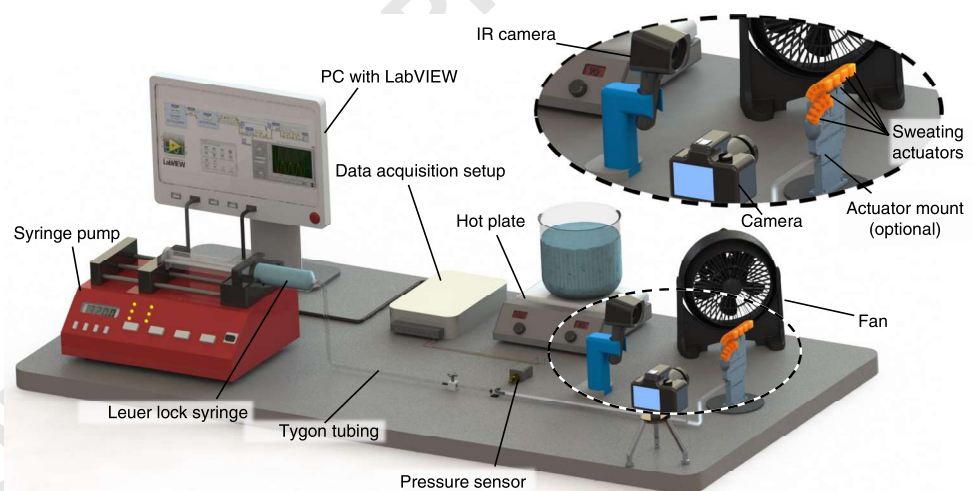

Fig. 4 | Experimental setup for mechanical and sweating tests.

then on the anthropomorphic soft hand (see Fig. 3a,b and Supplementary Figs. 6–9c for the design   516
schematics and reference [50]).   517

!CAUTION Use appropriate protective gear (oven mitts and tongs) to avoid damage from   518
manipulating hot objects.   519

▲CRITICAL STEP Conduct these experiments in a controlled environment. Particularly, reduce   520
erratic convective currents and maintain a constant temperature and relative humidity. Minimize   521
conductive losses by mounting the actuator on a stand (see the Supplementary Information and   522
design files[50]).   523

29 Similar to the procedure described above (Mechanical performance of actuator), secure the actuator   524
assembly within the field of view of a thermal camera (Fig. 4).   525
▲ CRITICAL STEP Maintain a consistent distance between the actuator and the camera. In our case,   526
we kept this distance within 100 ± 10 cm.   527   Q17
▲ CRITICAL STEP To accommodate for passive cooling during experimental set up, it is   528
recommended to equilibrate at a higher temperature than the desired experimental range.   529
Working safely but rapidly also mitigates these unintended losses. We observed a temperature loss   530
of ~3–5 °C during setup.   531

30 Again, using the LabView program, start the syringe pump at a constant flow rate and immediately   532
begin recording the actuator with a thermal camera. Depending on the camera, this can either be   533
continuous video footage or periodic images at short time intervals (i.e., $t = 15$ s).   534
▲ CRITICAL STEP When taking periodic images, ensure that the metadata or the field of view   535
contains timestamps.   536

31 Continue recording the actuator performance as needed, or until the body temperature reaches   537
ambient. Repeat as necessary for statistical significance ($n \geq 3$).   538

32 Fabricate a geometrically identical but non-sweating actuator by removing the pores. Repeat Steps   539
1–4 to generate a comparative data set. Similarly, this protocol enables assessment of designs with   540
different pore shapes, sizes or densities.   542   Q18

Thermography under forced convection (optional)   543

▲ CRITICAL The purpose of these steps is to find out how cooling is influenced by the rate of   544
convection. This is done by using a fan to experimentally create sufficient ‚forced convection‘, to   545
dominate any contribution from 'free convection'.   546

33 Place a fan (Honeywell HT-900) parallel to the sweating plane of the actuator and ensure that the   547
resulting air current encompasses the entire actuator area.   548

34 Maintain a consistent, known wind speed (e.g., fan setting 1, wind speed = 5.3 m/s) and repeat   549
Steps 1–5 above. In total, at least four thermography data sets should exist: (i) free convection,   550
sweating actuator; (ii) free convection, non-sweating actuator; (iii) forced convection, sweating   551
actuator and (iv) forced convection, non-sweating actuator.   553

Thermal manipulation by robotic sweating gripper   554

▲ CRITICAL Eluting moisture from within the robotic body may lead to more advanced functions,   555
including thermal manipulation of objects. To quantify the ability to cool down gripped objects, we   556
recommend performing the following steps.   557

35 Assemble a sweating robotic gripper. This can most easily be done by affixing numerous 3D-printed   558
finger-like actuators (see Fig. 3c above and Supplementary Figs. 10 and 11 for design schematics   559
and ref. [50]) onto a chassis that properly aligns the 'fingers' and the associated fluidic controls (inlets,   560
tubing, etc.).   561

36 Thermally equilibrate the gripper and the desired object at the desired elevated temperature. The   562
thermal imaging camera can confirm equilibration.   563

37 Similar to Thermoregulatory performance of sweating actuators above, use the FLIR camera to   564
record the manipulated object and the sweating robotic gripper from a constant distance (i.e., 100 ±   565
10 cm) over a period of time. For comparison, conduct the same experiment with a non-sweating   566   Q19
equivalent gripper.   567
▲ CRITICAL STEP Ensure that the manipulated object possesses a similar emissivity to that of the   568
soft robotic gripper (ε ~0.95). The use of surface coatings (e.g., paint) can alter emissivity.   570

Analysis of thermographic images   571

38 After finishing the above experiments, upload the images onto a computer. FLIR cameras   572
simultaneously take thermographs and optical images. In a thermographic image, each pixel is   573
assigned a color on the basis of the measured temperature from its IR spectrum.   574

39 Import the images into image analysis software. We recommend the FLIR Tools software. Within   575
this application, we chose to view the data as FLIR MSX (Multi-Spectral Dynamic Imaging) to   576
enable greater clarity of object edges and boundaries. This proprietary format combines each   577
thermal image with its corresponding optical image without diluting the thermographic data.   578

40 Choose a color pallet for the thermal image (e.g., File → Add → Folder → Image → Palette → Iron   579
bow). In FLIR Tools, we recommend the Iron bow pallet because it is a general pallet ideal for   580

identifying thermal anomalies and body heat. Further enhance the contrast in the image by right- 581
clicking on the image and selecting 'Color Presentation'. The 'Histogram Equalized' option provides 582
the largest contrast by removing unused colors from the color scale. 583
▲ CRITICAL STEP By default, FLIR Tools software uses a dynamic color scale that depends on 584
the maximum and minimum temperature in the field of view. As the actuator cools, the maximum 585
temperature often drops, which alters the default color scale and prevents obvious comparisons 586
made between images. To aid in visual comparisons, manually define the maximum and 587
minimum temperature in the color scale for each image as the overall maximum and minimum 588
temperatures observed across the entire experiment (File → Add → Folder → Image → Color Bar 589
→ Max/Min). 590

41 Record the appropriate experimental parameters for the thermal image acquisition. In our example 591
above, we recommend the default setting: emissivity, $\varepsilon = 0.95$; relative humidity, $RH = 50\%$; 592
reference temperature, $RT = 20\ °C$; and distance, $d = 100\ cm$. 593

42 With the object's features well defined, select an area of interest with the appropriate selection tool 594
(rectangular box or elliptic shape). The FLIR software calculates the maximum, minimum and 595
average temperature of pixels bound by the selection. For quantitative analyses, we use the average 596
temperature. 597
▲ CRITICAL STEP Choose an 'area of interest' that is consistently visible in all images and 598
sufficiently representative of the body temperature. In some cases, especially when the robotic body 599
is bent, it can be difficult to use a single polygon or ellipse to cover the area of interest. We 600 Q20
recommend using multiple polygons to extract the accurate temperature profile over the entire area 601
of interest. 602

43 Repeat as necessary for each thermal image. Record the average body temperature and the time of 603
image acquisition to generate the time-temperature dataset. This protocol assumes that the surface 604
temperature is representative of the body temperature. The resistance to heat transfer within the 605 Q21
body must be much less than the resistance to heat transfer from the body to the environment; this 606
assumption is valid for small Biot numbers ($Bi < 0.1$). When estimating the Biot number, use ASTM 607
E1952 (Test Method for Thermal Conductivity and Thermal Diffusivity by Modulated Temperature 608
Differential Scanning Calorimetry) to measure the thermal conductivity of the actuator. 610

Estimation of cooling capacity from thermography 611
▲ CRITICAL Animal physiology literature often compares thermoregulation in terms of cooling power 612
per unit body mass (W/kg). Unlike the methods used in animal physiology experiments (described in 613
the Introduction), which incorrectly attribute all water loss as productive evaporative losses, our time- 614
temperature data permit direct estimation of the cooling power. The flow of heat from a body results in 615 Q22
a drop in body temperature according to Eq. 1. 616

$$\dot{Q}_{total} = mc_p \frac{dT}{dt} \tag{1}$$

Where $\dot{Q}$ is the instantaneous heat transfer rate (W), m is the mass of the system (kg) and c_p is the 618
specific heat ($J \bullet kg^{-1} \bullet °C^{-1}$). 619

44 Identify a temperature range (T_1–T_2) consistent with all trials from the thermographic data. 620

45 For each dataset, determine the times (t_1 and t_2) that correspond to these temperature values. 621
▲ CRITICAL STEP When making discrete thermographic measurements (i.e., thermal images and 622
not thermal videos), there can be gaps in the time-temperature data that prevent an exact 623
thermograph corresponding to the desired points (t, T). Here, we recommend using the adjacent 624
data points ($t_i > t > t_j$) to linearly interpolate an estimate of these values. 625

$$t = t_i + (t_j - t_i) * \frac{(T - T_j)}{(T_i - T_j)}$$
$$or \tag{2}$$
$$T = T_i + (t - t_j) * \frac{(T_i - T_j)}{(t_i - t_j)}$$

627

46 If unknown, measure the specific heat capacity, c_p, for the materials following an appropriate 628
measurement protocol such as ASTM E1269[51]. 629
▲ CRITICAL STEP For multimaterial construction, measure the specific heat capacity of each of the 630
base components. Estimate the effective heat capacity as a weighted average (by mass) of the 631
individual heat capacities. Include the pressurizing fluid in these calculations. 632

47 From the time, temperature and specific heat data, calculate the cooling power by using   633
    Eq. (3) below.   634

$$Cooling\ Power\left(\frac{W}{kg}\right) = \frac{\dot{Q}}{m} = \frac{c_p[T_2 - T_1]}{[t_2 - t_1]} \tag{3}$$

636

▲**CRITICAL STEP** This estimate captures all modes of heat transfer (conductive, convective,   637
radiative and evaporative). To isolate the contribution from sweating, subtract the cooling power of   638
an equivalent non-sweating actuator.   640

Lumped parameter analysis   641

▲**CRITICAL** According to Newton's Law of Cooling, the rate of heat flow depends on the device   642
geometry and the thermal gradient between body temperature and that of the ambient environment   643
(T_a). Thus, comparisons between instantaneous cooling rates are valid only over similar experimental   644
conditions. To enable quantitative comparisons across experimental trials (e.g., to compare cooling   645
capacities of different machines or starting temperatures), we propose the use of a 'lumped parameter'.   646
For a more thorough justification of this derivation, see the previously published report[52–54].   647

$$\frac{dT}{dt} = -b(T - T_a) \tag{4}$$

where b is our lumped parameter. We impose the boundary condition that $T = T_0$ at $t = 0$. Solving   649
this first-order differential equation yields the analytical model (Eq. 5):   650

$$T(t) = (T_0 - T_a)e^{-bt} + T_a \tag{5}$$

Newton's Law of Cooling holds only for certain situations, like forced air–driven convection with a   652
constant heat transfer coefficient. To date, there is no multiphysics model that could simultaneously   653
describe this system's conductive, radiative, convective and evaporative modes of heat transfer. As such,   654
the lumped parameter, b, does not carry any phenomenological meaning—it merely quantifies an   655
equivalent idealized scenario, where the cooling rate is linearly proportional to the temperature gradient.   656

48 Identify a consistent T_0 from the experimental data. Ideally, choose the lowest initial 'average body   657
    temperature' found among the different trials. Because body temperature is a state function, this   658
    ensures that the range of data will overlap.   659

49 For each dataset, determine the starting time (t_0) that corresponds to this T_0 value. Appropriately   660
    shift the time values in the dataset to such that $t_0 = 0$.   661
    ▲**CRITICAL STEP** Again, discontinuous sampling may preclude direct observation of the desired   662
    initial data point (t_0, T_0) across all trials. Similar to the above (Eq. 2), for the chosen initial body   663
    temperature (T_0), interpolate the appropriate starting time (t_0) from the neighboring values.   664

50 Plot T versus t and fit the data for an exponential decay according to Eq. 4 above. Extract the   665
    lumped variable, b. If desired, determine the R value of these fits more than 0.96.   666 Q23

51 Repeat for the other experimental conditions. When comparing systems, higher lumped parameters   667
    indicate increased cooling rates.   669

Troubleshooting

670

Troubleshooting advice can be found in Table 3.   671

Table 3 | Troubleshooting table

Step	Problem	Possible reason	Solution
5	Object failing to print	Underpolymerization	Increase photo-exposure dosage by 10% and reprint. For any alteration to the resin's composition, we recommend generating a new working curve
	Loss in z-axis resolution, excessive cure-through, printer jamming	Overpolymerization	Decrease the photo-exposure time by 10% or add non-reactive absorptive species (nanoparticles or dyes). For any alteration to the resin's composition, we recommend generating a new working curve
			Table continued

Table 3 (continued)

| Step	Problem	Possible reason	Solution
	A printed part is breaking or deflecting during printing	Mechanical translations during printing are greater than the yield strength of the part	Realign the part such that the principle axes are parallel to the incident forces (i.e., translations of the build head)
	A printed part exhibits poor x-y resolution but maintains acceptable z-resolution	The active free species diffuses beyond the photo pattern; it usually coincides with an increase in resin viscosity over the print process	Increase the amount of radical scavenging species (hydroquinone). In addition, increasing the wait period (ModelPressWaitMS) or the z-axis separation (ModelZLiftMicrons) between layer exposures helps drain partially cured resin from within intricate features
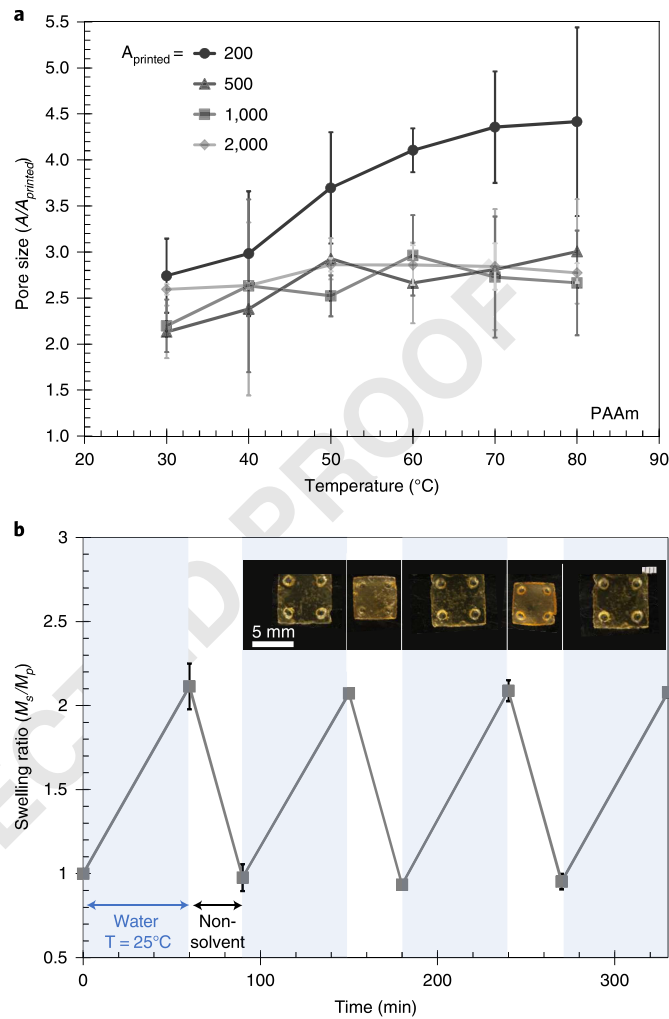
Fig. 5 | Dynamic response of hydrogel pores. a, Dimension change of PAAm-based pores of different diameters in response to temperature. **b**, Reversibility of hydrogel response in favorable and unfavorable conditions. Error bars represent the standard deviation ($n \geq 7$). Reproduced with permission from ref. [33].

Q25

Timing

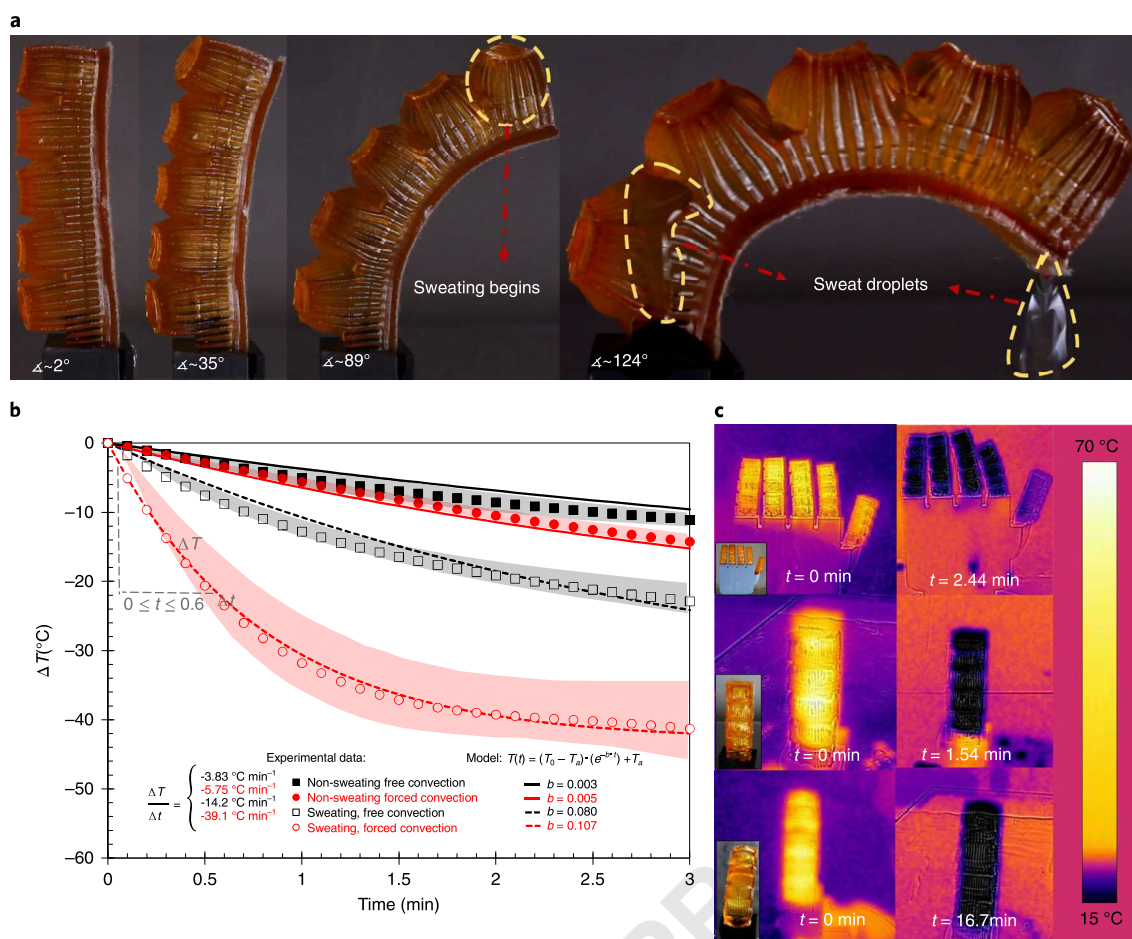Steps 13–18, characterization of smart materials for autonomic pores: ~24 h

672
673 Q24

Fig. 6 | Performance of sweating actuators. a, An actuator pressurized to different actuation angles and sweating. **b**, The temperature change of sweating (dashed lines) and non-sweating (solid lines) actuators under both free (black) and forced (red) convection modes. Shaded regions represent the range of temperature over three trials. **c**, A robotic hand composed of sweating actuators rapidly thermoregulating via perspiration.

Anticipated results

674

675 This protocol outlines the design and manufacture of FEAs that perspire. Stereolithographic printing
676 of hydrogel chemistries yields bioinspired soft robots with dynamic micropores that autonomically
677 dilate and contract in response to temperature. As shown in Fig. 5a, appropriate material selection
678 and design should yield pores that exhibit a significant change (>25%) in cross-sectional area with
679 temperature. For stable autonomic operation, this dimensional change should be reversible. As shown
680 in Fig. 5b, our hydrogel system is capable of undergoing numerous dilation and contraction cycles
681 between favorable (water, 25 °C) and unfavorable (non-solvent) conditions.

682 In Fig. 6a, we showcase an example actuator printed according to the above protocol and pres-
683 surized to obtain different actuation amplitudes during perspiration. In Fig. 6b, we measured the
684 surface temperatures for these sweating actuators (solid lines) and their non-sweating actuators
685 (dashed lines) in an environment with free convection (black lines) and forced convection (red lines).
686 Our perspiring finger-like actuators initially cooled up to 39.1 °C/min under forced convection (wind
687 speed = 0.165 m^3/s), whereas the same non-sweating variant dropped only −5.75 °C/min over the
688 same conditions. Through this comparison, we estimate that perspiration increases the effective
689 lumped parameter, b, by 0.102, which corresponds to a 1.6-W increase in cooling capacity.

Q26

690 Researchers can perform sanity checks to verify the feasibility of their measured perspiration-based
691 cooling capacity by crudely tracking the water economy. The water loss rate (ml/s) multiplied by the
692 molar density of water (55 mmol/ml) and enthalpy of vaporization (~40.65 kJ/mol) yields the
693 maximum possible heat loss from evaporation only (W). Our results above (1.6 W of CEWL from
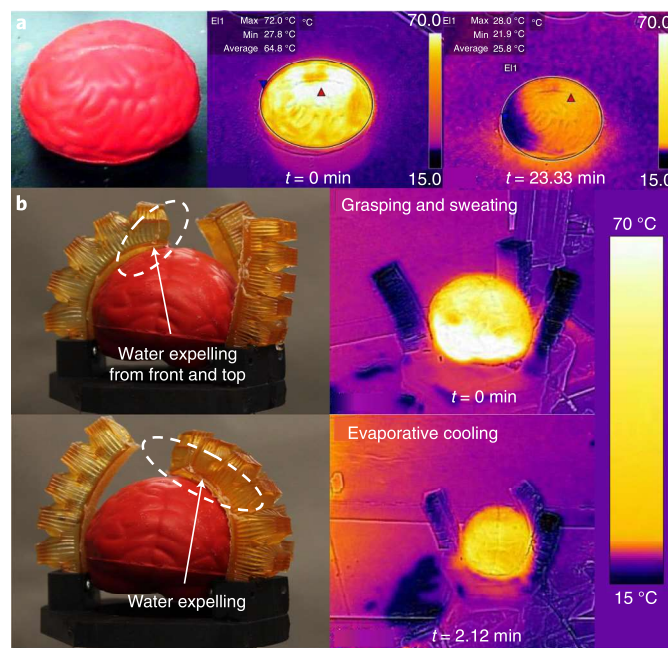694 sweating) suggest an evaporative water loss of ~0.04 ml/min, a plausible value that is consistent with

Fig. 7 | Thermo-manipulation of grasped objects. a, A polyurethane foam object passively cooling in air. **b**, The same polyurethane foam object rapidly cooling because of secreted perspiration from the robotic gripper composed of sweating actuators.

empirical observations. For large-scale systems, tracking the volume of water in the internal reservoir or the overall mass of the system could provide direct measurements of the water loss rate. Liquid water probably leaves the surface of the actuator before evaporation; this water loss is not productive for thermoregulation. Modifications to surface texture, pore density, pore distribution, etc. can reduce this inefficient water loss.

However, these water droplets that fall from the actuator's surface can be used to cool their surroundings to enable thermo-manipulation. In Fig. 7a, a polyurethane foam object is shown passively cooling under ambient conditions. By comparison, in Fig. 7b, the same object is being thermo-manipulated by a robotic gripper composed of perspiring actuators. The secreted water from the gripper rapidly cools the surface of the object, to improve cooling rates by >200%.

Reporting Summary

Further information on research design is available in the Nature Research Reporting Summary linked to this article.

References

1. Kim, S., Laschi, C. & Trimmer, B. Soft robotics: a bioinspired evolution in robotics. *Trends Biotechnol.* **31**, 287–294 (2013).
2. Trivedi, D., Rahn, C. D., Kier, W. M. & Walker, I. D. Soft robotics: biological inspiration, state of the art, and future research. *Appl. Bionics Biomech.* **5**, 99–117 (2008).
3. Laschi, C., Mazzolai, B. & Cianchetti, M. Soft robotics: technologies and systems pushing the boundaries of robot abilities. *Sci. Robot.* **1**, eaah3690 (2016).
4. Laschi, C. & Cianchetti, M. Soft robotics: new perspectives for robot bodyware and control. *Front. Bioeng. Biotechnol.* **2**, 3 (2014).
5. Ilievski, F., Mazzeo, A. D., Shepherd, R. F., Chen, X. & Whitesides, G. M. Soft robotics for chemists. *Angew. Chem. Int. Ed. Engl.* **50**, 1890–1895 (2011).
6. Iida, F. & Laschi, C. Soft robotics: challenges and perspectives. *Procedia Compute. Sci.* **7**, 99–102 (2011).
7. Highton, H. Perpetual motion. *Nature* **3**, 368–369 (1871).
8. Shepherd, R. F. et al. Using explosions to power a soft robot. *Angew. Chem. Int. Ed. Engl.* **52**, 2892–2896 (2013).
9. Marchese, A. D., Onal, C. D. & Rus, D. Towards a self-contained soft robotic fish: on-board pressure generation and embedded electro-permanent magnet valves. In *Experimental Robotics* **Vol. 88** (eds. Desai, J., Dudek, G., Khatib, O. & Kumar, V.) 41–54 (Springer, Heidelberg, Germany, 2013).

10. Bartlett, N. W. et al. A 3D-printed, functionally graded soft robot powered by combustion. *Science* **349**, 161–165 (2015).
11. Miriyev, A., Stack, K. & Lipson, H. Soft material for soft actuators. *Nat. Commun.* **8**, 1–8 (2017).
12. Yirmibeşoğlu, O. D., Oshiro, T., Olson, G., Palmer, C. & Mengüç, Y. Evaluation of 3D printed soft robots in radiation environments and comparison with molded counterparts. *Front. Robot. AI* **6**, 40 (2019).
13. Tolley, M. T. et al. A resilient, untethered soft robot. *Soft Robot.* **1**, 213–223 (2014).
14. (!!! INVALID CITATION!!! {\,}).
15. Grady, J. M., Enquist, B. J., Dettweiler-Robinson, E., Wright, N. A. & Smith, F. A. Evidence for mesothermy in dinosaurs. *Science* **344**, 1268–1272 (2014).
16. Wright, P. Why do elephants flap their ears? *Afr. Zool.* **19**, 266–269 (1984).
17. Farlow, J. O., Thompson, C. V. & Rosner, D. E. Plates of the dinosaur Stegosaurus: forced convection heat loss fins? *Science* **192**, 1123–1125 (1976).
18. Kotagama, P., Phadnis, A., Manning, K. C. & Rykaczewski, K. Rational design of soft, thermally conductive composite liquid-cooled tubes for enhanced personal, robotics, and wearable electronics cooling. *Adv. Mater. Technol.* **4**, 1800690 (2019).
19. Morin, S. A. et al. Camouflage and display for soft machines. *Science* **337**, 828–832 (2012).
20. VII. Scala graduum caloris. *Philos. Trans. R. Soc. Lond.* **22**, 824–829 (1701).
21. Padilla, L. R. & Hilton, C. D. Canidae. In *Fowler's Zoo and Wild Animal Medicine* Vol. 8 (eds. Miller, R. F. & Fowler, M. E.) 457–466 (Elsevier Saunders, St. Louis, MO, USA, 2015).
22. Calder, W. A. & Schmidt-Nielsen, K. Temperature regulation and evaporation in the pigeon and the roadrunner. *Am. J. Physiol.* **213**, 883–889 (1967).
23. Dawson, W. R. Evaporative losses of water by birds. *Comp. Biochem. Physiol. A Physiol.* **71**, 495–509 (1982).
24. Dawson, M. E., Schell, A. M., Beers, J. R. & Kelly, A. Allocation of cognitive processing capacity during human autonomic classical conditioning. *J. Exp. Psychol. Gen.* **111**, 273–295 (1982).
25. Whitfield, M. C., Smit, B., McKechnie, A. E. & Wolf, B. O. Avian thermoregulation in the heat: scaling of heat tolerance and evaporative cooling capacity in three southern African arid-zone passerines. *J. Exp. Biol.* **218**, 1705–1714 (2015).
26. Ingram, D. Evaporative cooling in the pig. *Nature* **207**, 415–416 (1965).
27. Sawka, M. N., Wenger, C. B. & Pandolf, K. B. Thermoregulatory responses to acute exercise-heat stress and heat acclimation. *Compr. Physiol* **Suppl. 14**, 157–185 (2011).
28. Johnson, J. & Proppe, D. In *Handbook of Physiology, Section 4: Environmental Physiology* (eds. Fregly, M. J. & Blatteis, C. M.) (Oxford University Press Inc, New York, NY, USA, 1996).
29. Hodgson, D. et al. Dissipation of metabolic heat in the horse during exercise. *J. Appl. Physiol.* **74**, 1161–1170 (1993).
30. Kalairaj, M. S., Banerjee, H., Lim, C. M., Chen, P.-Y. & Ren, H. Hydrogel-matrix encapsulated Nitinol actuation with self-cooling mechanism. *RSC Adv.* **9**, 34244–34255 (2019).
31. Kozuki, T. et al. Skeletal structure with artificial perspiration for cooling by latent heat for musculoskeletal humanoid kengoro. In *2016 IEEE/RSJ International Conference on Intelligent Robots and Systems (IROS)* 2135–2140 (IEEE, Piscataway, NJ, USA, 2016).
32. Asano, Y., Okada, K. & Inaba, M. Design principles of a human mimetic humanoid: humanoid platform to study human intelligence and internal body system. *Sci. Robot.* **2**, eaaq0899 (2017).
33. Mishra, A. K. et al. Autonomic perspiration in 3D-printed hydrogel actuators. *Sci. Robot.* **5**, eaaz3918 (2020).
34. Banerjee, H., Suhail, M. & Ren, H. Hydrogel actuators and sensors for biomedical soft robots: brief overview with impending challenges. *Biomimetics (Basel)* **3**, 15 (2018).
35. Fan, H. & Gong, J. P. Fabrication of bioinspired hydrogels: challenges and opportunities. *Macromolecules* **53**, 2769–2782 (2020).
36. Wallin, T., Pikul, J. & Shepherd, R. 3D printing of soft robotic systems. *Nat. Rev. Mater.* **3**, 84–100 (2018).
37. Holback, H., Yeo, Y. & Park, K. Hydrogel swelling behavior and its biomedical applications. In *Biomedical Hydrogels: Biochemistry, Manufacture and Medical Applications* (ed. Rimmer, S.) 3–24 (Woodhead Publishing Limited, Cambridge, UK, 2011).
38. Ebara, M. et al. *Smart Biomaterials*. (Springer, Tokyo, Japan, 2014).
39. Yuk, H. et al. Hydraulic hydrogel actuators and robots optically and sonically camouflaged in water. *Nat. Commun.* **8**, 1–12 (2017).
40. Ge, Q. et al. Multimaterial 4D printing with tailorable shape memory polymers. *Sci. Rep.* **6**, 31110 (2016).
41. Odent, J. et al. Highly elastic, transparent, and conductive 3D-printed ionic composite hydrogels. *Adv. Funct. Mater.* **27**, 1701807 (2017).
42. Wallin, T. et al. Click chemistry stereolithography for soft robots that self-heal. *J. Mater. Chem. B* **5**, 6249–6255 (2017).
43. Peele, B. N., Wallin, T. J., Zhao, H. & Shepherd, R. F. 3D printing antagonistic systems of artificial muscle using projection stereolithography. *Bioinspir. Biomim.* **10**, 055003 (2015).
44. Hunter, J. *Observations on Certain Parts of the Animal Economy*. (London, UK, 1792).
45. Taylor, C. R. Strategies of temperature regulation: effect on evaporation in East African ungulates. *Am. J. Physiol.* **219**, 1131–1135 (1970).
46. Ohhashi, T., Sakaguchi, M. & Tsuda, T. Human perspiration measurement. *Physiol. Meas.* **19**, 449–461 (1998).

47. Kingston, J., Geor, R. & McCutcheon, L. Use of dew-point hygrometry, direct sweat collection, and measurement of body water losses to determine sweating rates in exercising horses. *Am. J. Vet. Res.* **58**, 175–181 (1997).
48. *Flir E4 Brochure*. Available at https://www.flir.com/globalassets/imported-assets/document/ex-series-no-wifi-datasheet.pdf (2020).
49. Bennett, J. Measuring UV curing parameters of commercial photopolymers used in additive manufacturing. *Addit. Manuf.* **18**, 203–212 (2017).
50. Mishra, A. K. P., Wenyang, P., Giannelis, E. P., Shepherd, R. F. & Wallin, T. J. Stl files for 3D printed Sweating actuators 09/17/2020 edn. Available at https://figshare.com/articles/dataset/Stl_files_for_3D_printed_Sweating_actuators/12964811 (2020).
51. ASTM International. *Standard Test Method for Determining Specific Heat Capacity by Differential Scanning Calorimetry*. (ASTM International, West Conshohocken, PA, USA, 2011).
52. Rajput, R. *Heat and Mass Transfer in SI Units*. 98–99 (S. Chand & Company Ltd., 2008).
53. Incropera, F. P., DeWitt, D. P., Bergman, T. L. & Lavine, A. S.*Fundamentals of Heat and Mass Transfer* (Wiley, 2007).
54. Nag, P. *Engineering Thermodynamics* (Tata McGraw-Hill Education, 2013).

792
793
794
795
796
797
798
799
800
801 Q32
802
803 Q33
804 Q34
805
806 Q35
807 Q36

Acknowledgements

808
809
810
811

Data availability

The data used in this protocol are available in the supporting primary research article, and the design files are accessible at https://doi.org/10.6084/m9.figshare.12964811.

812 Q27
813
814

Software availability

The MATLAB code used in this protocol can be found in the Supplementary Information files.

815
816

Competing interests

The authors declare no competing interests.

817
818 Q28

Additional information

Supplementary information The online version contains supplementary material available at https://doi.org/10.1038/s41596-020-00484-z.

Correspondence and requests for materials should be addressed to T.J.W.

Peer review information *Nature Protocols* thanks Dacheng Wei and the other, anonymous, reviewer(s) for their contribution to the peer review of this work.

Reprints and permissions information is available at www.nature.com/reprints.

Publisher's note Springer Nature remains neutral with regard to jurisdictional claims in published maps and institutional affiliations.

819
821
823
824
825
826
827
828
829
830
831

832
833

Related links
Key reference using this protocol
Mishra, A. et al. *Sci. Robot.* **5**, eaaz3918 (2020): https://doi.org/10.1126/scirobotics.aaz39181038